International Journal of Heat and Mass Transfer 194 (2022) 122987

Contents lists available at ScienceDirect

International Journal of Heat and Mass Transfer

journal homepage: www.elsevier.com/locate/hmt

A graph-theory based directed network feature for thermal anisotropy

Wenbin Fei[a], Qirui Ma[b,c], Kenichi Soga[d], Guillermo A. Narsilio[a,*]

[a] Department of Infrastructure Engineering, The University of Melbourne, Engineering Block B, Parkville, VIC 3010, Australia
[b] Changjiang Institute of Survey, Planning, Design and Research, Wuhan 430010, China
[c] State Key Laboratory of Water Resources and Hydropower Engineering Science, Wuhan University, Wuhan 430072, China
[d] Department of Civil and Environmental Engineering, The University of California, Berkeley, CA 94720, USA

ARTICLE INFO

Article history:
Received 24 November 2021
Revised 11 April 2022
Accepted 29 April 2022
Available online 24 May 2022

Keywords:
Heat transfer
Thermal anisotropy
Thermal network
Microstructure
Contact orientation
Soil fabric

ABSTRACT

The effective thermal conductivity of a granular material varies with the predominant heat transfers direction. The anisotropic effective thermal conductivity is known to be dominated by the microstructure in a dry material. However, no microstructural parameters that are well related to thermal anisotropy have been proposed. After analysing the heat transfer mechanisms at the particle scale, this work constructs new directed weighted thermal networks for both lattice and randomly distributed sphere packings, by considering particles as nodes and local heat transfer paths with thermal resistance as directed edges. With the implementation of graph theory to the directed weighted thermal networks, the shortest preferential heat transfer paths between nodes paired at opposite faces of a sample across the driving temperature gradient direction are identified. Based on the shortest heat transfer paths, a new sample-scale feature named "*directed network thermal resistance*" is computed for each sample. This new parameter accounts for particle connectivity, interparticle contact orientation and contact quality simultaneously. After computing the effective thermal conductivity of each sample in different directions using a weighted thermal network model, it is found that directed network thermal resistance is inversely proportional to anisotropic effective thermal conductivity.

1. Introduction

Heat transfer in porous media is crucial in a wide range of industries such as, geothermal systems [1], carbon dioxide geological storage [2], coal bed methane extraction [3] and granular bed [4]. Effective thermal conductivity λ_{eff} is a parameter used for quantifying the heat transfer rate through a material. A shallow geothermal system utilises porous geomaterials such as soils and sands as a heat source to warm a building in the winter or a heat sink to cool a building in the summer. The λ_{eff} of a geomaterial can vary in different directions due to geological consolidation. For example, the λ_{eff} of the Opalinus clay is 1.55 W/(m K) when measuring parallel to its bedding direction, which is double the λ_{eff} perpendicular to the bedding direction [5]. This large difference could dominate the design of the geothermal system in a site, since a vertical geothermal system requires high horizontal λ_{eff} while a horizontal system needs high vertical λ_{eff}. The heat transfer rate varying in different directions is called thermal anisotropy. In an energy pile system that allows a building to use pile foundations to exchange heat with soil/rocks, pile driving induces the deformation of soils surrounding the pile and hence increasing the thermal anisotropy of soils [6]. In deep geothermal engineering, the convection of high-temperature water and steam aggravate the thermal anisotropy of fractured and layered rocks [7]. The above engineering scenarios highlight the significance of studying thermal anisotropy in geomaterials.

The λ_{eff} of a geomaterial at rest depends on its interior microstructure. However, plenty of conventional [8–10] and more advanced artificial neural network models [11–13] for λ_{eff} prediction consider sample-scale porosity as the sole microstructural parameter. Smaller particle-scale and meso-scale microstructural parameters such as particle shape and particle connectivity were not included in the models although extensive research presented their importance to heat transfer. For a packing made of elongated particles, its λ_{eff} is significantly higher when heat transfers through the long-axial direction than that through the short-axial direction [14]. In addition, the roughness of the particle surface increases the thermal anisotropy of an ellipsoid assembly since roughness increases the number of contact points along the minor axes than that on the major axes of the ellipsoids [15].

A contact between two particles can be characterised in various aspects such as contact number (i.e. coordination number), contact quality (e.g. contact area or thermal resistance) and contact orien-

* Corresponding author.
E-mail address: narsilio@unimelb.edu.au (G.A. Narsilio).

https://doi.org/10.1016/j.ijheatmasstransfer.2022.122987
0017-9310/

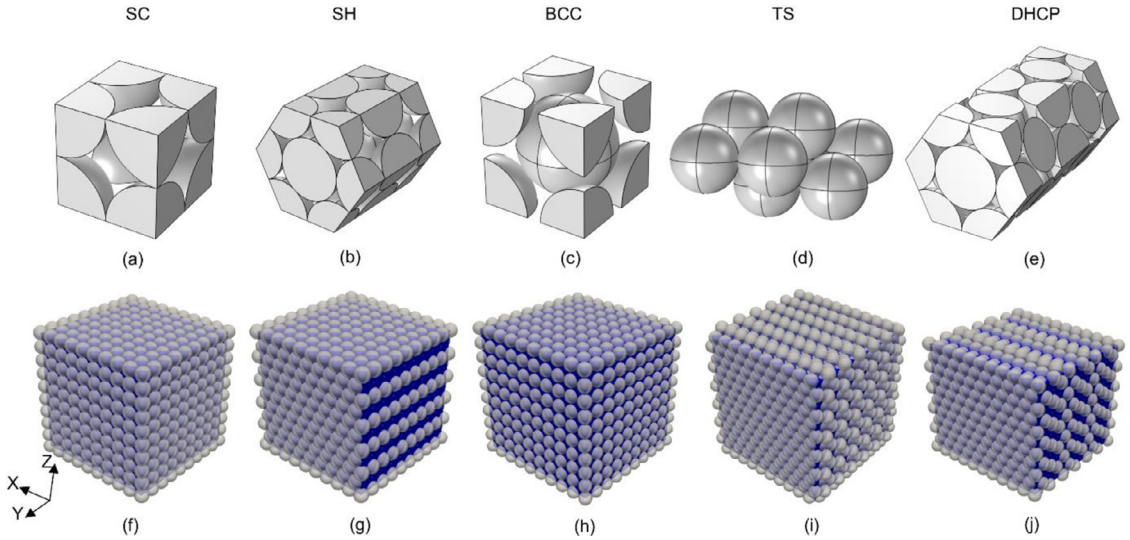

Fig. 1. The unit cells of the regular packings studied: SC (a), SH (b), BCC (c), TS (d) and DHCP (e) alongside the corresponding packings of SC (f), SH (g), BCC (h), TS (i) and DHCP (j).

tation (i.e. contact angle). The change of contact number and contact quality along heat transfer direction affects thermal anisotropy. Wang et al. [16] discovered that the connectivity of particles along the heat transfer direction could be a preferential heat transfer path. Therefore, it is an economical way to improve heat transfer by concentrating the contacts of particles along the thermal gradient [17,18]. Even embedding a small percentage of long particles with high thermal conductivity and aligning their long axis with temperature gradient can improve λ_{eff} by 30% [19]. In a sample under deformation, the topology/fabric and contact area are also related to the deformation-induced thermal anisotropy [20]. Despite the observed importance of contact to thermal anisotropy, no direct relationship between microstructural parameters and thermal anisotropy has been established because of the lack of directed microstructural parameters.

Graph theory, also known as complex network theory, is a powerful mathematical tool based on networks to quantify the particle arrangement [21,22], pore connectivity [23], force transmission [24] and heat transfer [25] at multiple scales. Its application to granular materials enriches the family of microstructural parameters, especially addressing the issue of scarcity in characteristic parameters available to quantify particle connectivity. Coordination number may be one of the few parameters available to date for such a task. A contact network of particle packing can be built by assigning a node for each particle and generating an edge if two particles are in contact. Contact area can also be incorporated into each edge to form a weighted contact network from which network features extracted cover both particle connectivity and contact quality. Similarly, a weighted thermal network can be constructed by further generating near-contact edges if two adjacent particles have a small gap, and incorporate thermal conductance instead of contact area to each edge for the weighting. The features from the networks are well correlated to λ_{eff} of isotropic materials [25,26]. However, the application of graph theory to investigate thermal anisotropy is still an untouched research topic.

This paper aims to use graph theory to find a microstructural parameter that relates to thermal anisotropy well. Both lattice sphere packings and randomly distributed sphere packings were created. While the existing networks used in the study of porous media are typically undirected (i.e., the edge from node *i* to node *j* is the same as the edge from node *j* to node *i* in an undirected network), directed weighted thermal networks were constructed for each sample in this paper, meaning that edges in this new networks are affected by the predominant heat transfer direction (i.e., the external driving temperature gradient) and local thermal conductance. This allowed to identify preferential heat transfer paths and compute a new sample scale thermal resistance R from each new thermal network. Finally, the relationship between R and λ_{eff} along different heat transfer directions for each regular (lattice) packing were investigated.

2. Granular assemblies

Regular sphere packings as well as randomly distributed sphere packings were built for this study. Details of each are summarised in this section.

2.1. Lattice sphere packings

Simple cubic (SC), simple hexagonal (SH), body centred cubic (BCC), tetragonal sphenoidal (TS) and double hexagonal closed-packed (DHCP) are five lattice structures that were selected in this work to build sphere packings, and their unit cells are shown in Fig. 1(a–e). SH is a hexagonal prism with an atom on each of 12 corners and both faces. TS is a sphere packing with one special rhombic face and two rhombic faces [27]. DHCP has a 4-layer stacking pattern ABAC-ABAC. The relatively large sphere packings (Fig. 1(f–j)) consisting of different lattice structures have different coordination numbers (CN) and porosity (Table 1). Note all the sphere packings were intentionally constructed as hexahedrons (Fig. 1(f–j)) in this study rather than stacking multiple unit cells (Fig. 1(a–e) together to calculate the λ_{eff} in x, y and z directions. SC and BCC are isotropic samples and used to check the algorithms of computing the new directed thermal resistance. The boundaries of other samples are not in line with the symmetry crystallographic axes, but samples were considered to be larger enough to investigate the anisotropy of thermal conductivity without many errors being introduced.

Based on the SC lattice (Fig. 1(a)), 1000 spheres of diameter 1.31 mm were arranged with a distance of 1.3 mm between the centroids of each two neighbouring spheres, resulting in a sample (Fig. 1(f)) with a CN of 5.4 computed using Eq. (1) and porosity of 0.477 considering the void volume in the blue block displayed in Fig. 1(f). The sample size is large enough for heat transfer

Table 1
Lattice sphere packings information.

Sample	SC	SH	BCC	TS	DHCP
Theoretical coordination number	6	8	8	10	12
Theoretical porosity	0.476	0.395	0.320	0.302	0.260
Particle number in the packing	1000	1050	1729	1876	1502
Coordination number in the packing	5.4	7.1	6.7	8.8	10.5
Porosity in the packing	0.477	0.394	0.343	0.304	0.261
Length in mm (L_x)	11.70	11.70	13.51	13	13
Width in mm (L_y)	11.70	11.70	13.51	13.51	12.74
Height in mm (L_z)	11.70	11.26	13.51	13.51	11.26

Note: each sphere has diameters of 0.13 mm and a distance of 0.131 mm from its centroids to its neighbours. Dimensions of a sphere packing were measured using the blue block in Fig. 1.

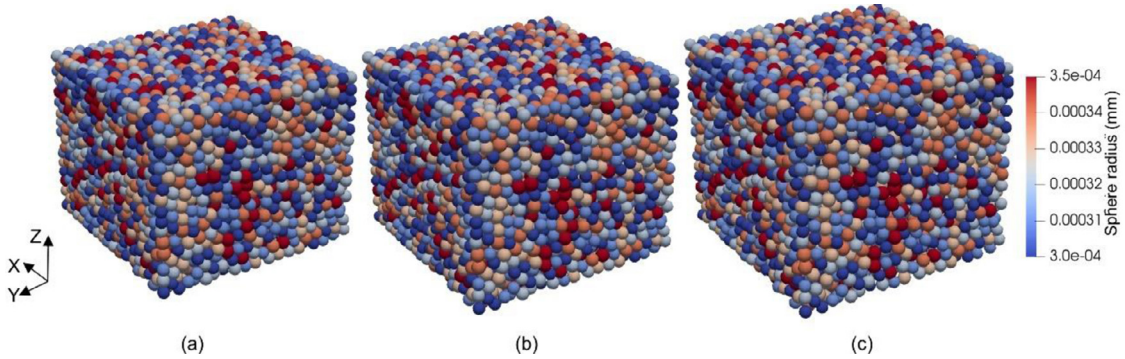

Fig. 2. DEM samples with porosity of 0.2 (a), 0.3 (b) and 0.4 (c).

simulation in granular materials compared with 211 spheres used in the paper [28]. The other packings were similarly built. Table 1 summarises key information for each of the constructed packings. The unit cell of SH and DHCP are hexagonal prisms if symmetric boundaries are desired. Since the large sphere packings of SH and DHCP are hexahedrons as shown in Fig. 1(b) and (e) instead of hexagonal prisms, the same sphere pattern is used on the opposite boundaries of SH/ DHCP along an axis to achieve some periodicity, as shown in Fig. 1(g) and (j).

$$CN = 2 \cdot \frac{Contact\ number\ of\ all\ particles\ in\ the\ packing}{Particle\ number\ in\ the\ packing} \tag{1}$$

2.2. Randomly distributed sphere packings

Compared with lattice sphere packings in which spheres are located in order, randomly distributed sphere packings are more commonly encountered in nature and geotechnical engineering applications. In this work, randomly distributed sphere packings varying in porosity, as shown in Fig. 2, were generated using Liggghts [29], an open-source discrete element method (DEM) particle simulation software. In the DEM simulation, 5968 spheres with radii of 0.3–0.35 mm were first randomly located in a relatively large cube with an edge length of 15 mm. Next, the planes of the cube are moved inwards along the vertical (z) direction at a higher rate than the horizontal (x and y) directions. The z-directional velocity is set 1.5 times higher than that at x- and y-directions to induce an anisotropic microstructure of the packing. Five samples with different porosities, 0.2, 0.25, 0.3, 0.35 and 0.4 were constructed. The inclusion of the rolling friction coefficient in a DEM simulation can result in a strong force network that is orientated firmly along the major stress direction and can make the sample more heterogenous after deformation .A rolling friction coefficient was set as 0.2 in this work to ensure a realistic particle rotational frustration [30]. Other DEM simulation parameters are summarised in Table 2.

Table 2
Simulation parameters used in DEM.

Parameters	Values
Density (kg/m^3)	2600
Young's modulus (GPa)	1
Poisson's ratio	0.2
Particle number in the packing	5968
Sphere radius (mm)	0.3–0.35
Friction coefficient	0.5
Rolling friction coefficient	0.2

3. Directed network feature

Since a network is the basis for computing network features (or network parameters), this section introduces the heat transfer mechanisms with analogous resistors to indicate the potential of using directed weighted thermal networks to analyse heat transfer. The new network considers inter-particle contact orientation and uses the thermal resistance as the weight for each network edge. The computation of thermal resistance of resistors is introduced, followed by the details of constructing a directed thermal network. At last, a network feature from the network is extracted to quantify the directed thermal resistance of a sample.

3.1. Heat transfer analysis using resistors

The λ_{eff} of a sample can be computed by using Fourier's law (Eq. (2)):

$$\lambda_{eff} = \frac{\frac{1}{A}\sum Q_{ij}}{(T_{inlet} - T_{outlet})/L} \tag{2}$$

where A is the cross-section area of the sample in the direction perpendicular to heat transfer (the major temperature gradient direction), $\sum Q_{ij}$ is the sum of the heat flux Q_{ij} at each edge (i-j) intersecting the cross-section plan, T_{inlet} and T_{outlet} are the boundary temperature at inlet (i.e., "high" temperature) and outlet (i.e.,

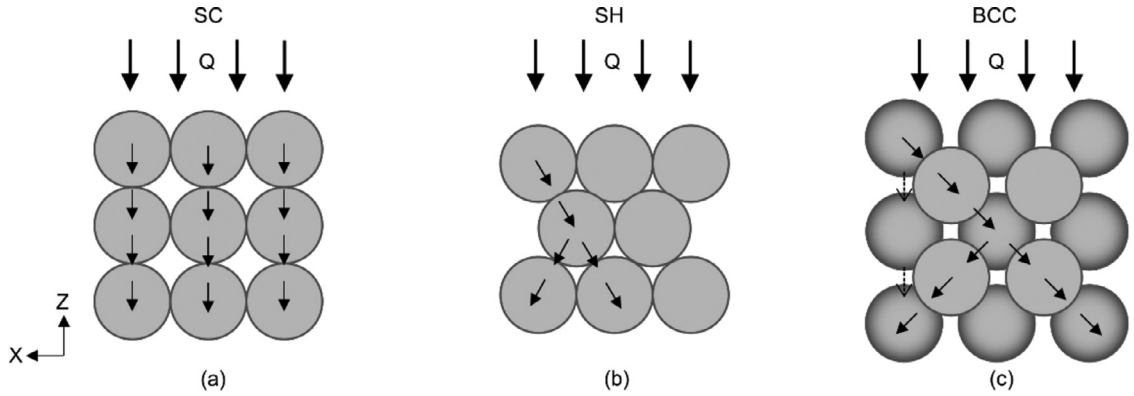

Fig. 3. Schematic heat conduction paths in lattice sphere packing SC (a), SH (b) and BCC (c). Solid arrows in particles represent heat transfer in particle and via interparticle contacts, while dash arrows indicate heat transfer through particle-fluid-particle.

"low" temperature) planes of the sample, L is the sample length along the predominant heat transfer direction. Hence, for different samples with the same temperature gradient $(T_{inlet} - T_{outlet})/L$, their λ_{eff} is directly proportional to the heat flux density $\frac{1}{A}\sum Q_{ij}$ on a given boundary plane.

The mechanisms of heat transfer in dry granular materials include heat conduction, convection and radiation. Air flows slowly when air pressure is less than 0.15 MPa and the corresponding convection is negligible [31]. Furthermore, heat radiation is usually ignored at a temperature lower than 1000 K [32]. Hence, heat convection and radiation are ignored in dry granular geomaterials (e.g., sands) in this paper. In dry granular geomaterials, heat flux between two particles is concentrated near interparticle contact or near-contact [33,34]. Hence, the temperature within a particle could be treated as uniform if the solid is assumed as a perfect conductor, and then Eq. (3) can be used to compute the heat conduction between particles:

$$Q_{ij} = \frac{1}{R_{ij}}\left(T_i - T_j\right) \tag{3}$$

where Q_{ij}, R_{ij} are the heat flux and thermal resistance between node i at a temperature T_i and node j at a temperature T_j, respectively. According to Eq. (3), heat would not transfer between particles on the same plane that is perpendicular to the predominant heat transfer direction, since their temperatures would be the same. For example, heat only travels vertically rather than horizontally in the SC sample (Fig. 3(a)) when a vertical (z) temperature gradient is prescribed (i.e., horizontal x-y planes are isothermal planes). This analysis hints that the characterization of the microstructural topology in the heat transfer direction is required to quantify thermal anisotropy. By comparing the SC and SH (Fig. 3(b)) samples, their difference of $\frac{1}{A}\sum Q_{ij}$ is attributed to the heat transfer paths density between the boundary particles on the inlet and outlet faces when a vertical temperature gradient is prescribed. As for the BCC sample (Fig. 3(c)), the heat transfer paths densities also depends on the heat transfer direction. Hence, the heat transfer paths are required to be identified to calculate their density.

Widely used microstructural parameters such as porosity is a characteristic at the macro-scale, which has no direct relationship with the heat transfer path. The coordination number quantifies the number of connections between a particle and its neighbours, but the effect of contact direction on temperature difference is not included. For example, the coordination numbers in the vertical (z) and horizontal (x and y) directions in SC are the same, but the contacts perpendicular to the heat transfer direction do not contribute to the heat flux in Eq. (3).

Additionally, one reason for the difficulty of characterizing thermal conduction in soils is that heat conducts in both solid and fluid phases, compared to fluid flow only in pore space and force transmission only through solids. The particle-fluid-particle conduction shown as dash arrows in (Fig. 3(c)) has not been characterized by coordination number and other traditional microstructural parameters.

Inspired by Eq. (3), a resistor was used to present the heat transfer path between two particles, as shown in Fig. 4(a). Resistors were not created at the contacts that are perpendicular to the main (macro-scale) heat transfer direction since one may not expect a high temperature difference and heat flux through the contacts. Next, for each particle at the inlet boundary (top x-y boundary plane in this example), a paired particle on the outlet boundary (bottom x-y plane) was found if the in-series resistors between the two inlet and outlet particles have the smallest resistance. The in-series resistors could be presented as long inlet-outlet resistors as shown in Fig. 4(b).

All generated long inlet-outlet resistors connect the paired inlet and outlet particles in parallel, which relates to the contribution of the particle to the $\sum Q_{ij}$ in Eq. (2). The parallel inlet-outlet resistors can be used to calculate a sample-scale resistance R, which is named "*directed network thermal resistance*" in this paper. The topology of the resistors in a sample can be abstracted using a directed network by considering each particle is a node and each resistor is an edge. The thermal resistance of each resistor is considered as the weight to be added to each edge. In the next section, we will show how the thermal resistance is calculated.

3.2. Thermal resistance computation

Heat conduction in dry granular materials occurs via three main paths: (1) within particles, (2) through interparticle contacts when two particles are in touch and (3) through near-contacts, which are small gaps between neighbouring particles as shown in Fig. 5(a). For sphere packings, particles in contact are represented as two particles that overlapped with a (flat surface) contact radius r_c. This assumption is widely used in DEM software [35,36].

Batchelor and O'Brien [34] proposed expressions for local thermal conductance that is the reciprocal of thermal resistance in particles, between particles in and near in contact, by approximating heat flux across two particles through as a cylindrical conductor of equivalent radius r_{ij} (Fig. 5(b)). In other words, heat flux in particle packings are hindered by (thermal) resistances within the particle itself (R_n^P), at the contact between neighbouring particles ($R^{contact}_{ij_{interparticle}}$) and to a lesser degree at the "small enough" void gaps between particles in the packing ($R^{contact}_{jk_{gap}}$). These resistances can

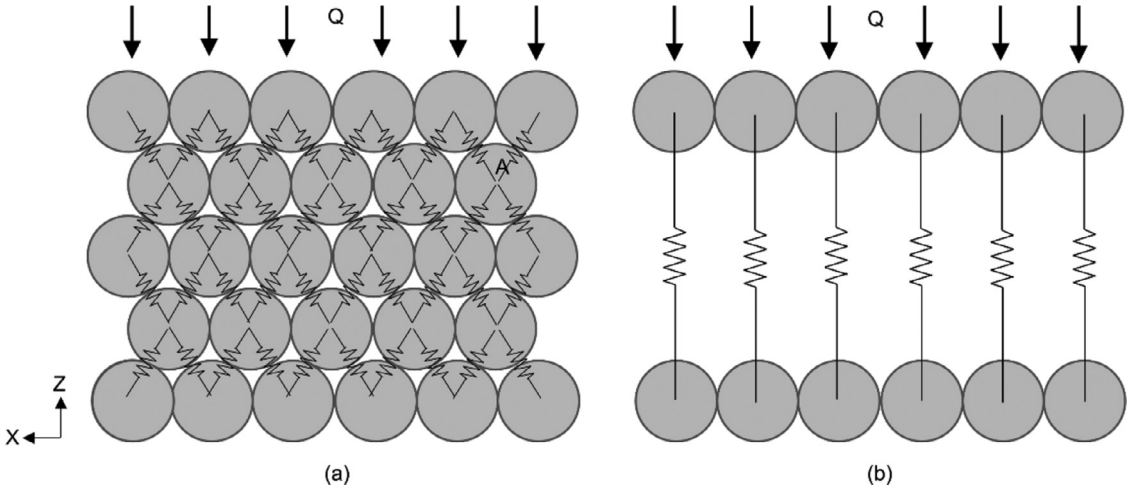

Fig. 4. The implementation of conductor to represent heat transfer between two neighbouring particles (a) and pairs of particles at the inlet (top) and outlet (bottom) boundaries.

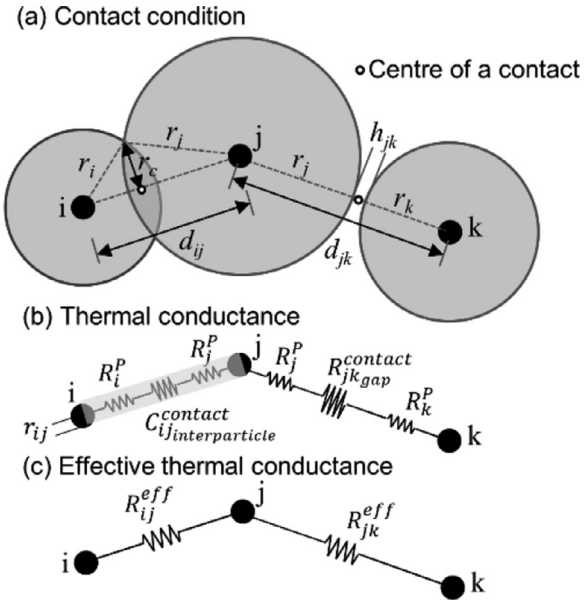

Fig. 5. Contact conditions (a) and the associated local thermal conductance (b) were used to compute the effective thermal conductance between two particles (c).

be idealised as occurring through cylindrical bodies of equivalent thermal resistance (or reciprocal conductance) and can be approximated as follows (see [34] and implementations in e.g., [26,37,38]):

- **Thermal resistance within a particle is:**

$$R_n^P = \frac{r_n}{\pi \lambda_s \left(r_{ij}^c\right)^2}, \quad n \in [i, j] \tag{4}$$

where $r_n (n \in [i, j])$ is the radius of particle i or j; λ_S is the thermal conductivity of solid particles; r_{ij}^c is an effective value of the radius r_{ij} of the equivalent cylinder (Fig. 5(b)). It is known that temperature distribution in a particle with finite thermal conductivity depart from uniformity at the contact point and then spread out [34]. This pattern is affected by the particle curvature, which is considered by adjusting r_{ij} in Eq. (5):

$$r_{ij}^c = \chi \cdot r_{ij} = \chi \frac{2 r_i r_j}{r_i + r_j} \tag{5}$$

where χ is the estimate of the fraction of the equivalent cylinder radius, and it is set to 0.5 in this work following the verification for sands in paper [37]. Its value could be 0.6–0.8 when studying the λ_{eff} of packed pebble beds with the consideration of the reduction of gas thermal conductivity due to the decrease of gas pressure on (i.e., Smoluchowski effect) [39,40].

- **Thermal resistance between overlapped particles with a contact radius of r_c is:**

$$R_{ij_{overlap}}^{contact} = \left(\pi \cdot \lambda_v \cdot r_{ij} \cdot \left[\lambda_c + \Delta\lambda_g + \ln\left(\alpha^2\right)\right]\right)^{-1} \tag{6}$$

where λ_v is the thermal conductivity of fluid in void space.

$$\begin{cases} \lambda_c = \frac{2\beta_{ij}}{\pi} and\ \Delta\lambda_g = -2\ln\left(\beta_{ij}\right)\ if\ \beta_{ij} \to \infty \\ \lambda_c = 0.22\beta_{ij}^2\ and\ \Delta\lambda_g = -0.05\beta_{ij}^2\ if\ \beta_{ij} < 1 \end{cases} \tag{7}$$

where β_{ij} is an overlap parameter related to the thermal conductivity ratio $\alpha = \lambda_s/\lambda_v$.

$$\beta_{ij} = \alpha \cdot \frac{r_c}{r_{ij}} = \frac{\lambda_s}{\lambda_v} \cdot \frac{r_c}{r_{ij}} \tag{8}$$

- **Thermal resistance between particles near in contact (i.e. with a small gap h_{jk}):**

If the $h_{jk} < \epsilon \cdot R_{jk}$ where ϵ is the cutoff parameter to define the maximum distance that heats conduction between particle j and k via fluid in the void; ϵ was set as 0.5 following the verification for sands in paper [37].

$$R_{jk_{gap}}^{contact} = \begin{cases} \left(\pi \cdot \lambda_v \cdot r_{jk} \cdot \ln\left(\alpha^2\right)\right)^{-1}\ if\ \kappa_{jk} \ll 1 \\ \left(\pi \cdot \lambda_v \cdot r_{jk} \cdot \ln\left(1 + \chi^2 \cdot R_{jk}\right)\right)^{-1}\ otherwise \end{cases} \tag{9}$$

where κ_{jk} is a sphere separation parameter and defined as:

$$\kappa_{jk} = \frac{\alpha^2 \cdot h_{jk}}{r_{jk}} \tag{10}$$

By considering the local heat transfer paths as resistors in series, the effective thermal resistance can then be computed as:

$$R_{ij}^{eff} = \begin{cases} R_i^P + R_{ij_{overlap}}^{contact} + R_j^P\ if\ in\ contact \\ R_j^P + R_{jk_{gap}}^{contact} + R_k^P\ if\ in\ near-contact \end{cases} \tag{11}$$

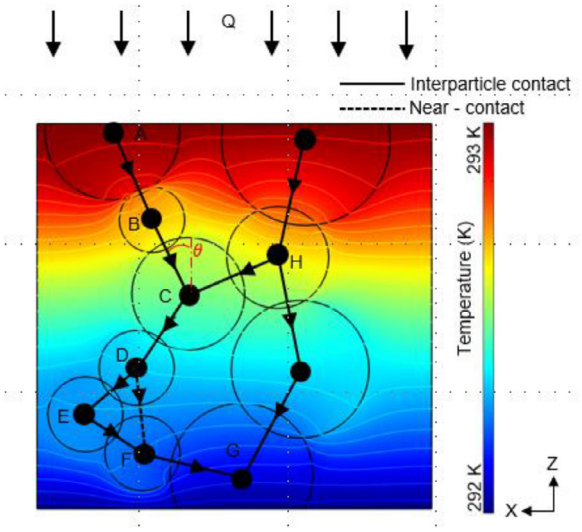

Fig. 6. Schematic illustration of constructing a directed thermal network (temperature field computed using FEM to better illustrate temperature gradients).

3.3. Directed thermal network construction

In an undirected thermal network in our previous work [25,26], a node represents a particle while an edge represents an interparticle contact or a near-contact. Since heat travels from high temperature to low temperature, the direction should be considered when searching the in-series resistors from thermal inlet to outlet particles, especially in randomly distributed sphere packings. In a directed thermal network shown in Fig. 6, the shortest heat transfer path is A-B-C-D-E-F-G. If the direction was not considered, the shortest heat transfer path would be incorrectly identified as A-B-H-G. In this work, the direction of a network edge is determined by the coordinates of the two nodes at the ends of the edge. Here we assume a close correlation between particle position and temperature distribution (and heat flux direction) which is reasonable for lattice and random packings. For example, if the main heat transfer direction is downward along the z-axis in Fig. 6, H to C is likely to be the correct direction of edge HC since H has a larger z value (and higher temperature) than C. While this would not hold true if the participle on top of H were not there (and particle C would have higher temperature than particle H, thus reversing the heat flux direction to be C-H), this loss of particle connectivity is unlikely to occur in random packings subjected to gravity (and compressive stresses), thus the simple use of particle position to determine (thermal) edge direction. For contacts that are perpendicular to the main heat transfer direction, no edges were generated since the temperature difference through the contacts are zero.

In addition, thermal resistance at an interparticle contact could be ten times smaller than that at a near-contact in a dry granular material since the thermal conductivity of a solid mineral could be 3 W/(m K) [33,37] while the thermal conductivity of air is 0.025 W/(m K) [41]. If neglecting the resistance, the local path D-F could be incorrectly recognised as a shortcut. Furthermore, since an angle θ exists between an edge and the main heat transfer direction (e.g. from top to bottom in Fig. 6), the thermal resistance R_{ij}^{eff} computed from Eq. (11) at an edge should be penalised by multiplying $cos\theta$ since the thermal resistance of a resistor is proportional to its length. The penalised thermal resistance at each contact was employed as a weight for each network edge, finally resulting in a directed weighted thermal network.

3.4. Directed network thermal resistance computation

As presented in Fig. 4(b), each paired inlet-outlet particles can be connected by a long inlet-outlet resistor that represents a preferential heat transfer path. If the resistance $R_{inlet-outlet}$ of each long inlet-outlet resistors is given, then the thermal resistance of the sample can be calculated as the reciprocal of the sum of reciprocals of the individual resistors using Eq. (12) since these long inlet-outlet resistors are in parallel:

$$R = \left(\sum \frac{1}{R_{inlet-outlet}} \right)^{-1} \tag{12}$$

Based on the constructed weighted directed thermal network, a python library for complex network theory (i.e., graph theory) called graph-tool [42] was used to identify the long thermal inlet-outlet resistors that consist of local resistors (i.e., each network edge) in-series (Fig. 4(a)). Graph-tool searches all the potential paths between the paired inlet and outlet particles and calculates the $R_{inlet-outlet}$ on the paths. The path with smallest $R_{inlet-outlet}$ was kept as the long inlet-outlet resistor.

After graph-tool finds the long inlet-outlet path with the lowest $R_{inlet-outlet}$, the next step is to check whether any local resistor on this path intersects with other local resistors, i.e., multiple pathways may intersect. If an intersection exists, partial heat transfer contributions from the other pathways are then accounted using the resistances of the intersected resistors recorded by graph-tool. For example, the long inlet-outlet path with the lowest $R_{inlet-outlet}$ in Fig. 6 is A-B-C-D-E-F-G, but path B-C meets path H-C at node C. The simple sum of the thermal resistances of the resistors on A-B-C-D-E-F-G would miss the contribution of heat on path H-C. Therefore, the thermal resistance of BC needs to be modified using Eq. (13) since BC and HC are in parallel:

$$R_{BC}^{eff\prime} = \frac{R_{BC}^{eff} R_{HC}^{eff}}{R_{BC}^{eff} + R_{HC}^{eff}} \tag{13}$$

This paper also considered the side boundary condition as symmetric when analysing heat transfer using thermal resistors. Only resistors with the centres of their corresponding contacts inside the blue box (Fig. 1) were considered in the calculation of the thermal resistance of the inlet-outlet resistors. The centre of an interparticle contact or near-contact (Fig. 5) was calculated using particle radii and the length of the related network edge. If the centre of a contact was at the side plane, the resistance of the related resistor was doubled. If the centre of a contact was at the corner of the box, the resistance was quadrupled, this way we account for symmetric temperature boundaries.

The considerations of resistor intersection and boundary condition update the resistances of local resistors on the long inlet-outlet resistor. Then, the $R_{inlet-outlet}$ of each inlet-outlet resistor is recomputed and used to calculate the thermal resistance R of the in Eq. (12).

4. Effective thermal conductivity computation

4.1. Thermal network model (TNM)

Existing work [37,38,43] used a thermal network model (TNM) based on an *undirected* weighted thermal network to compute the λ_{eff} of a sample. Substituting the computed effective thermal resistances R_{ij}^{eff} from Eq. (11) into Eq. (3), one can compute the heat flux Q_{ij} transferred between any two particles i and j if the temperature T of the two particles are given. Eq. (3) can be expressed

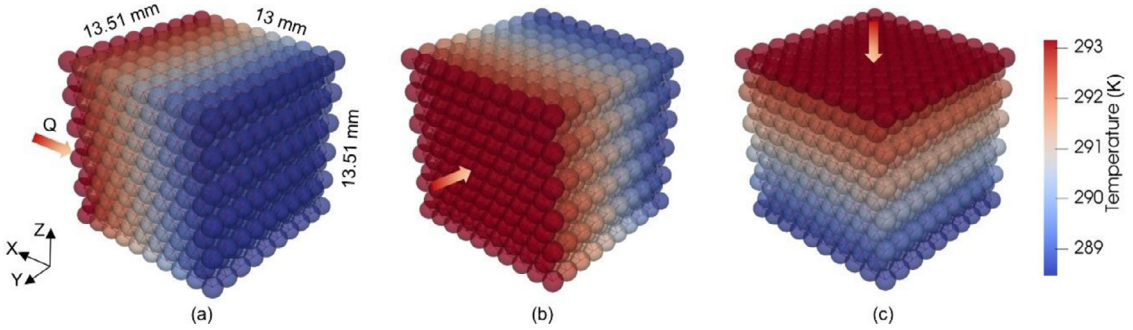

Fig. 7. Heat transfer simulation using thermal conductance network model along x (a), y (b) and z (c) directions.

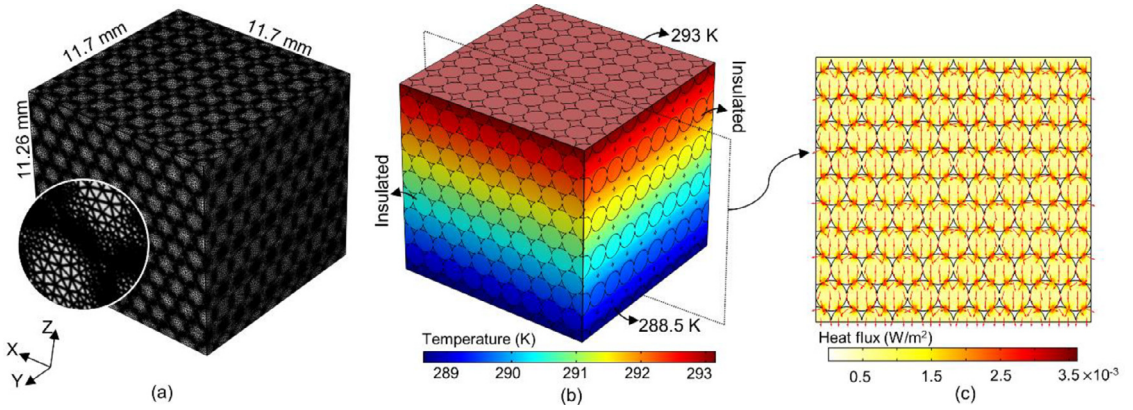

Fig. 8. Finite element simulation of SH packing. (a) meshes, (b) boundary conditions and resulting temperature distribution and (c) heat flow direction and heat flux distribution on a vertical cross-section.

in a matrix form as:

$$\begin{bmatrix} \frac{1}{R_{ij}^{eff}} & -\frac{1}{R_{ij}^{eff}} \\ -\frac{1}{R_{ij}^{eff}} & \frac{1}{R_{ij}^{eff}} \end{bmatrix} \begin{bmatrix} T_i \\ T_j \end{bmatrix} = \begin{bmatrix} C_{ij}^{eff} & -C_{ij}^{eff} \\ -C_{ij}^{eff} & C_{ij}^{eff} \end{bmatrix} \begin{bmatrix} T_i \\ T_j \end{bmatrix} = \begin{bmatrix} Q_{ij} \\ Q_{ji} \end{bmatrix} \tag{14}$$

where C_{ij}^{eff} is the thermal conductance between node i and j.

Then, the above local matrix for two particles can be extended to a global matrix for all particles in a sphere packing as in Eq. (15):

$$\boldsymbol{CT} = \boldsymbol{Q} \tag{15}$$

where $\boldsymbol{C}$ is the global thermal conductance matrix, $\boldsymbol{T}$ contains the temperature and heat flux at each particle and $\boldsymbol{Q}$ includes the heat flux between a paired two particles. Given the prescribed boundary temperature T_{inlet} at the inlet and T_{outlet} at the outlet boundaries of a sphere packing, the unknown particle temperatures in Eq (14) were solved. Then, Eq. (2) was used to calculate the λ_{eff} by substituting the archived Q_{ij} and other known parameters.

In this work, T_{inlet} was assigned a constant value of 293 K, T_{outlet} was computed using the same temperature gradient $\nabla T = 400$ K/m [37] for all the samples in Eq. (16).

$$T_{outlet} = T_{inlet} - \nabla T \times L \tag{16}$$

where L refers to Table 1. The temperature distribution in an SH packing is shown in Fig. 7. The edges are rendered in red to indicate heat conduction via the interparticle contact between every two neighbouring particles in SH packing.

4.2. Finite element simulation (FEM)

FEM is also used for heat transfer simulation and its results were compared with the λ_{eff} from TNM. The domains inside the blue blocks in Fig. 1(f–j) were imported to COMSOL Multiphysics [44] to generate geometry and meshes, as shown in Fig. 8(a) for SH packing. Its inlet and outlet were assigned the same boundary temperature as in TNM, while the side boundaries were assumed thermally insulated (Fig. 8(b)). The equations used to solve the heat transfer in granular materials can refer to our previous work [26].

Heat flux was computed during FEM simulation and its distribution is shown in Fig. 8(c), with heat flow direction presented as arrows. Heat flow arrows are concentrated at the interparticle contacts that are not parallel to heat transfer, resulting in maxima of heat flux there. This observation proves the correctness of the assumption when analysing heat transfer using thermal resistors in Section 3.1.

4.3. Theoretical models

Several widely accepted analytical expressions summarised in Table 3 were also used to verify the λ_{eff} from TNM. The analytical models such as series, parallel and Geometric mean, in essence, treat solid phase and void phase as two big thermal conductors/resistances. A similar logic but a more complex combination of thermal resistors were used for the heat analysis using conductors in this work (Fig. 4).

5. Results and discussion

5.1. Model verification

Effective thermal conductivity λ_{eff} from theoretical models (grey lines in Fig. 10) were used to verify the TNM model. In addition, the same samples were also used for FEM simulation in COMSOL Multiphysics. A mesh sensitivity analysis of the SC sample was conducted as shown in Fig. 9. It is found the λ_{eff} converges in models with more than 20 million finite elements. Hence

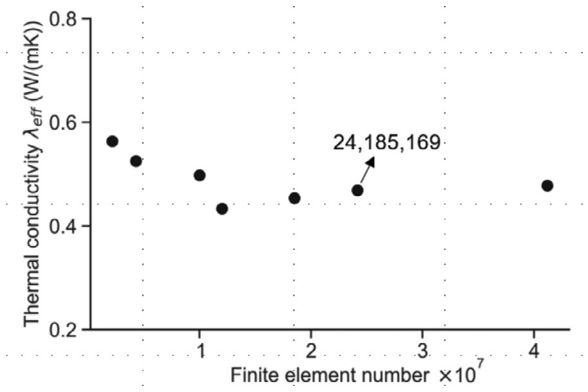

Fig. 9. Mesh sensitivity analysis for SC and models with different number of tetrahedra elements.

the COMSOL model with 24,185,169 tetrahedra elements was selected to compute the λ_{eff} of SC and its corresponding mesh size parameters were used to generate meshes for other samples. For all theoretical models, λ_{eff} is the same as the solid thermal conductivity when the porosity is 0; whereas λ_{eff} is the same as the void thermal conductivity when the porosity is 1. In general, all λ_{eff} computed from both FEM and TNM fall within the theoretical values, as shown in Fig. 10(a). Specifically, λ_{eff} computed from FEM is located between the Geometric mean model (GM) and the Self-consistent model (SC). The λ_{eff} from TNM models and is distributed around the GM curve and they are similar to the results from FEM.

After zooming in Fig. 10(a) and showing the x-directed λ_{eff} marked by lattice sample names in Fig. 10(b), most of the λ_{eff} in x direction calculated from TNM are above GM except for the λ_{eff} of BCC that is slightly below the GM. In contrast, most of the y-directed λ_{eff} from TNM shown in Fig. 10(c) are below the GM except for SC. Additionally, both the y-directed λ_{eff} from TNM and FEM decrease with the increase of porosity at a similar slope ratio of the GM curve, respectively. The deviation of their data from their own decreasing trend is smaller than that in x-direction (Fig. 10(b)) and z-direction (Fig. 10(d)). The small deviation is because the particles at the inlet and outlet of y-direction in each lattice sphere packings have the same *y* values, as shown in Fig. 1.

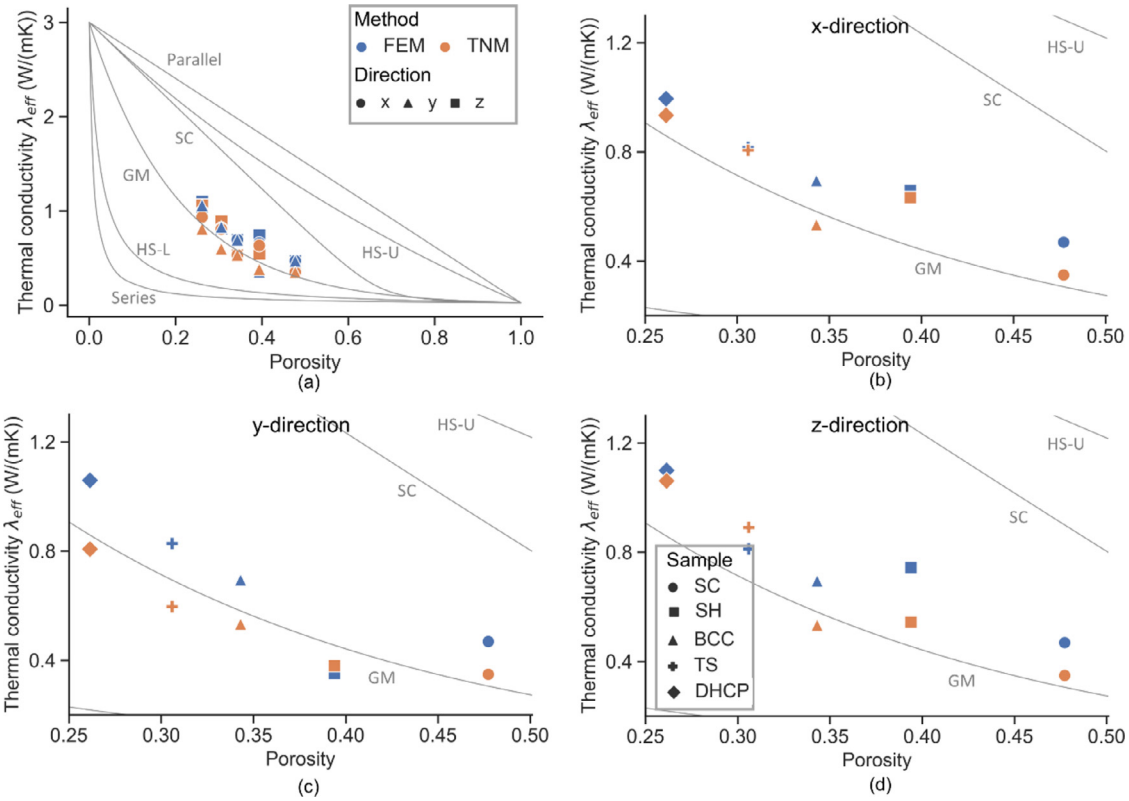

Fig. 10. Effective thermal conductivity λ_{eff} comparison from FEM, TNM and theoretical models: (a) λ_{eff} in all x, y and z direction, and the porosity is from 0 to 1; (b) a detailed subplot of (a) with λ_{eff} in x direction versus a narrower range of porosity; (c) λ_{eff} in y direction; (d) λ_{eff} in z direction. Note that the markers in (a) indicate the heat transfer direction while presenting different samples in (b),(c) and (d). The colours of makers in all figures indicate the methods.

Table 3
Theoretical models of predicting $\boldsymbol{\lambda_{eff}}$.

Model	Equation
Series [45]	$\lambda_{eff} = (\sum_{i=1}^{N} \frac{f_i}{\lambda_i})^{-1}$
Parallel [45]	$\lambda_{eff} = \sum_{i=1}^{N} f_i \cdot \lambda_i$
Geometric mean (GM) [46]	$\lambda_{eff} = \prod_{i=1}^{N} \lambda_i^{f_i}$
Hashin-Shtrikaman(HS-U: upper bound,HS-L: lower bound) [47]	$\lambda_{eff} = \lambda_1[1 + \frac{3f_2(\lambda_2-\lambda_1)}{3\lambda_1+f_1(\lambda_2-\lambda_1)}]$ (Upper: 1 = solid, 2 = pore;lower: 1 = pore, 2 = solid)
Self-consistent (SC) [48,49]	$\lambda_{eff} = \frac{1}{3}[\frac{1-n}{2\lambda_{eff}+\lambda_s} + \frac{n}{2\lambda_{eff}+\lambda_s}]^{-1}$

where λ_i is the thermal conductivity of the related phase occupying f_i in the sample, n is porosity.

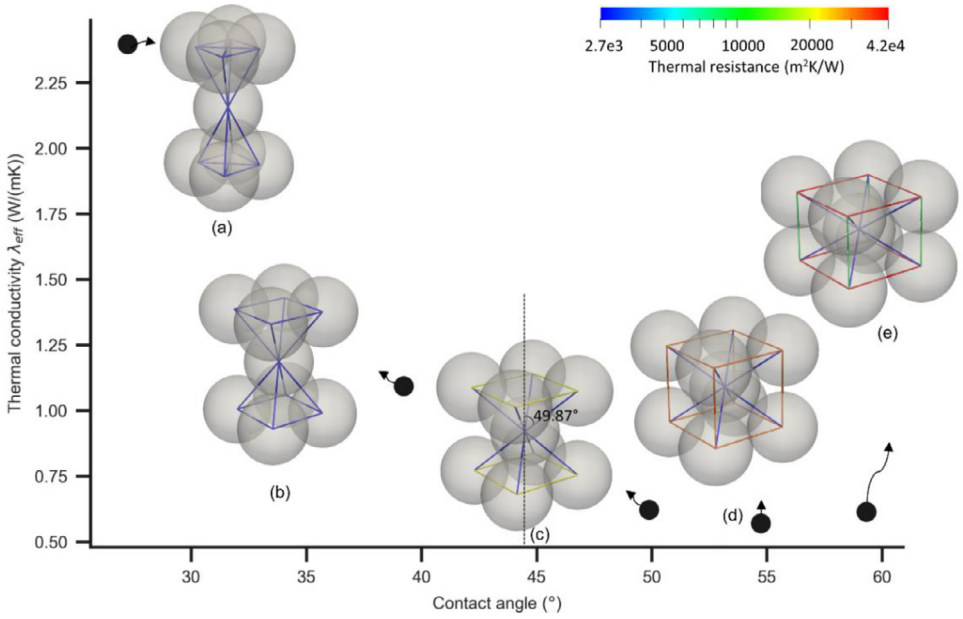

Fig. 11. Concat angle influence on λ_{eff} in BCC-like samples.

In other words, the centres of the inlet/outlet particles are on the blue inlet/outlet planes.

5.2. Effect of contact angle on effective thermal conductivity

The contact angle between a resistor axis and the main heat transfer direction was assumed to be important to the calculation of directed network thermal resistance R in Section 3.4. In this section, BCC-like sphere packings with different contact angles are used to analyse the impact of contact angle on λ_{eff}. From sample (a)–(e) in Fig. 11, the angle of the contacts between the central sphere and other spheres at corners to vertical direction varied, while the distance from centres of the particles diagonally in contact remained the same. Undirected networks with edges rendered by thermal resistance are also presented in the samples. λ_{eff} in vertical direction was computed using TNM. In sample (a)–(c) of Fig. 11, it can be seen that λ_{eff} experiences a sharp decrease from 2.39 to 0.62 W/(m K) when contact angle increases from 27.2° to 49.87°. The observation indicates that contacts incline away from the main heat transfer direction can hinder the heat transfer and result in a small λ_{eff}. It also proves that the essentiality of considering contact angle to construct a directed thermal network in Section 3.3.

From sample (c)–(d), four new near-contacts appear. Although their near-contact directions are the same as the main vertical heat transfer direction, the λ_{eff} still decreases when the interparticle contact direction increases from 49.87° to 54.73°. The decrease of λ_{eff} is because the thermal resistance of near-contacts is around 10-times larger than that of interparticle contacts. With the interparticle contact angle further increases to 59.31° in the sample (e), the λ_{eff} starts to increase because the resistance of near-contacts in sample (e) is only half of the value in the sample (d). The contribution of near-contacts to the increase of λ_{eff} indicates the necessity of including thermal resistance to build the weighted thermal network as explained in Section 3.3.

5.3. Directed network thermal resistance R and thermal anisotropy in ordered sphere packings

For each lattice sphere packing, both its directed and undirected thermal networks were constructed. The directed network was used to calculate the new proposed sample-scale directed thermal resistance R, while the undirected network was for computing λ_{eff}. To examine the robustness of the R when using it for predicting directed λ_{eff}, the thermal conductivity of solid is not only set as 3 W/(m K), but also as 1 W/(m K) of monazite and 8 W/(m K) of quartz [50].

A similar inversely proportional relationship between the directed R and λ_{eff} are shown in Fig. 12(a–c) even though the solid thermal conductivity varies. SC and BCC are two orthoisotropic

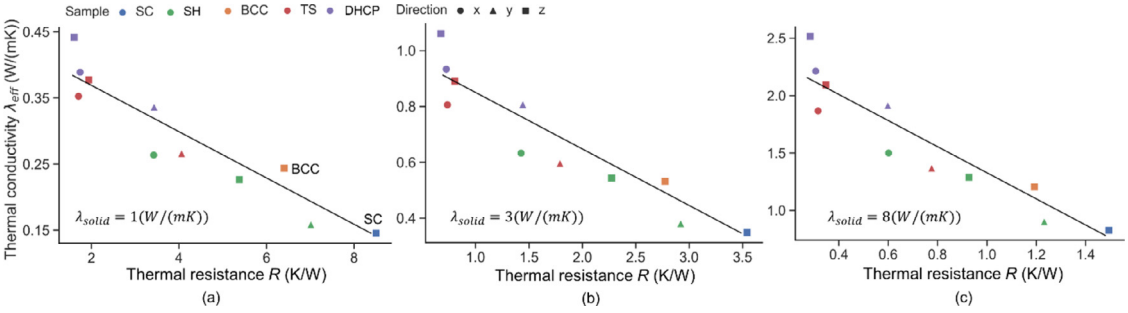

Fig. 12. Directed network thermal resistance R verses λ_{eff} of lattice sphere packings. Solid thermal conductivity is 1 W/(m K) in (a), 3 W/(m K) in (b) and 8 W/(m K) in (c) when calculating λ_{eff} in TNM.

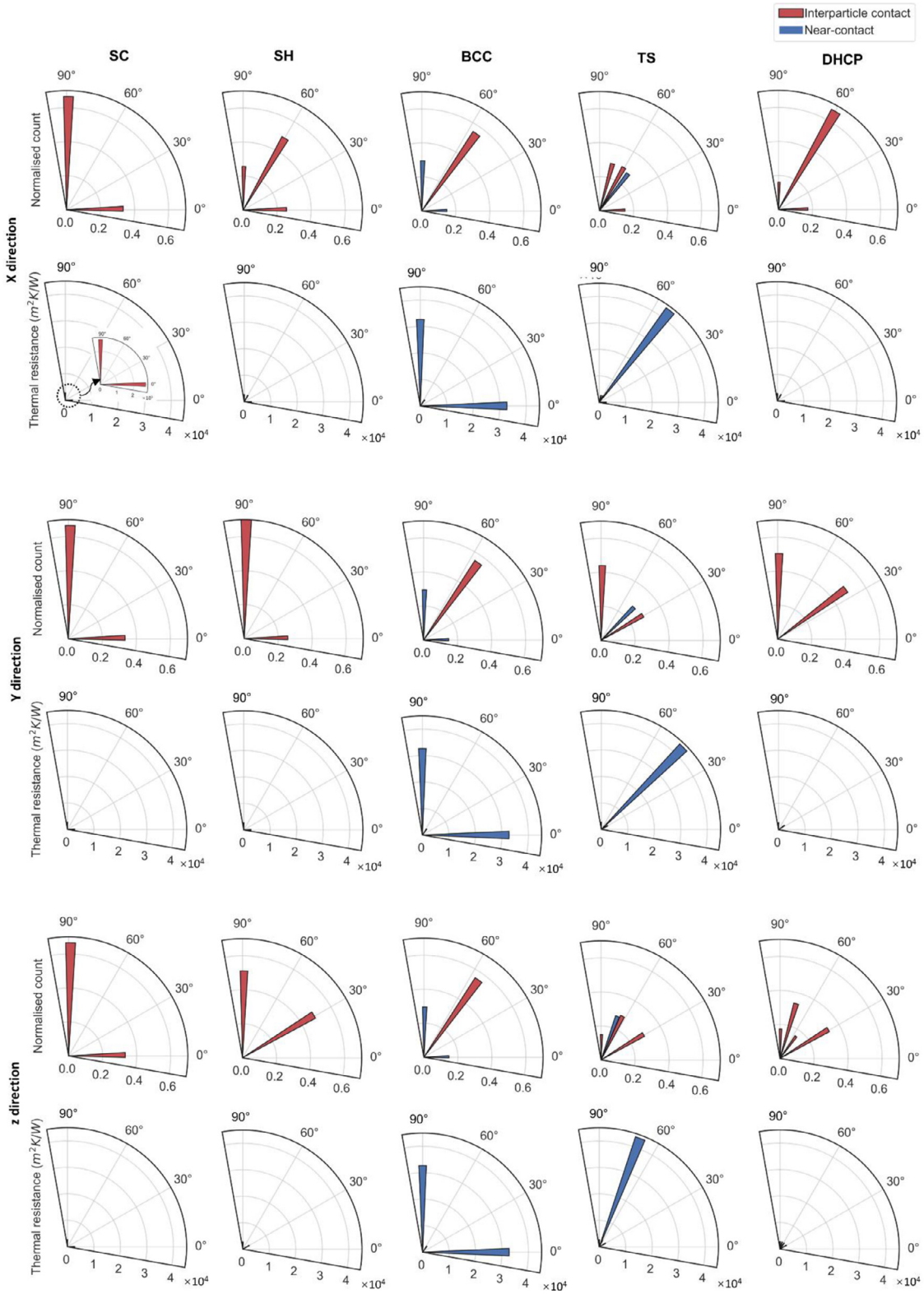

Fig. 13. Contact orientation and thermal resistance distribution in lattice sphere packings when heat transfers in x, y and z directions. Solid thermal conductivity is 3 W/(m K) when computing thermal resistance.

samples, their R and λ_{eff} are same in x, y and z directions, which indicates the correctness of computing R. The correlation between R and λ_{eff} of SH in different directions are well aligned with the general trend. In SH, the R in x-direction is around half of that in y-direction and 63% of that in z-direction, which is because of the different contact angles to different directions.

To investigate the contribution of contact orientation and local thermal resistance between neighbouring particles to R and anisotropic λ_{eff}, the number of contacts and the local thermal resistance along different orientations were displayed in rose diagrams as shown in Fig. 13. The orientation of a contact was defined as the angle between the main heat transfer direction and

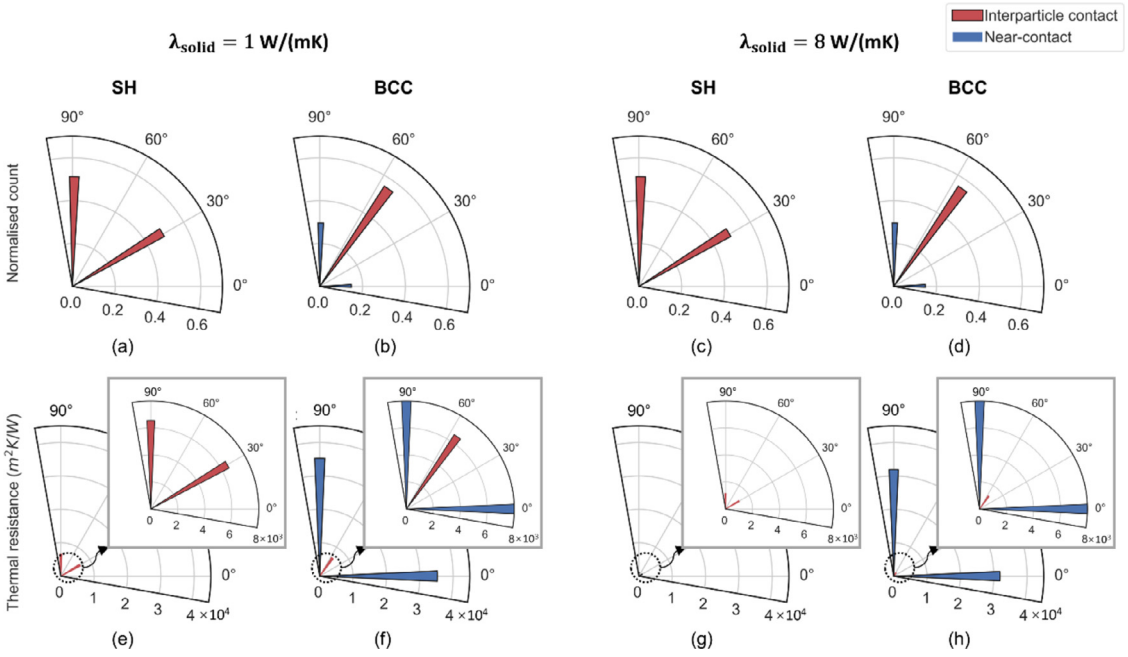

Fig. 14. Contact orientation and thermal resistance distribution in SH and BCC when heat transfers in z direction.

the axial direction of a network edge. Due to heat transfers in x, y and z directions, the relevant rose diagrams were plotted for each direction. As shown in Fig. 13, thermal resistances at all interparticle contacts of all lattice sphere packings are the same since the overlapped contact areas between two adjacent particles are designed the same during the sample construction. Only interparticle contacts exist in SH, around 25% of the contacts in SH are parallel to the x-direction (i.e. contact angle is 0°) with around 48% of contacts having a 60° angle to x-direction. In contrast, 50% of the contacts have no contribution to heat transfer in z-direction since they are perpendicular to z-axis (i.e. contact angle is 90°). The other 50% contacts dominate the heat transfer in z-direction, but their contact angle to z-direction is 30°.

DHCP has a similar unit cell as SH as shown in Fig. 1(b) and (e), but the middle vertical layer is rotated around y-axis in DHCP so that more contacts in DHCP have an angle of 60° to x-direction (Fig. 13), around 67% in DHCP while around 48% in SH. Although SH has more contacts parallel to x-direction, the significantly large amount of 60° contacts enables DHCP to have a larger λ_{eff} than SH. The large amount of 60° contacts to x direction in DHCP also makes a similar contribution to heat transfer compared with the contribution of a smaller amount of 30° and 73° interparticle contacts to heat transfer in z-direction.

In Fig. 12(a), the z-directional λ_{eff} of BCC is slightly larger than SH because near-contacts in BCC are parallel to z-direction as shown in Fig. 14(b) even though the interparticle contacts incline further away from z-direction (54.73°) than those of SH (30°). This observation indicates the importance of near-contacts to heat transfer, especially when the ratio of solid thermal conductivity to void thermal conductivity is small. However, the thermal resistance of interparticle contacts decreases from 6500 to 1150 m^2K/W when the thermal conductivity of solid increases from 1 to 8 W/(m K), the variation is larger than that of near-contacts (from 35,300 to 31,900). Hence, the contribution of 0° near-contact in BCC is overtaken by the 30° interparticle contacts in SH when the solid in the packings have larger thermal conductivity, resulting in the larger z-directional λ_{eff} of SH than that of BCC as shown in Fig. 12(b) and (c).

In Fig. 12, the R of TS in x-direction is smaller than its R in z-direction, and its λ_{eff} in x direction is also smaller than its λ_{eff} in z direction. This relationship between R and λ_{eff} is different from the general inversely proportional trend presented by black lines when considering the data from all samples in all three directions. The singularity is because the unit cell of TS shown in Fig. 1(d) has inclined side boundaries in x directions, which did not result in periodic boundaries as in other lattice samples. After visualising the particle arrangement of TS by scaling down the particle size, and the isothermal surface in FEM simulations in Fig. 15, it can be seen that spheres are arranged with a certain spacing in y-direction. Additionally, the spacings along with directions A and B in the yz view shown in Fig. 15(a) are the same. Hence, the isothermal surfaces are perpendicular to the main heat transfer direction (i.e. the y-direction) shown in Fig. 15(c). In contrast, the spacings along direction A are larger than that along direction B in the xz view (Fig. 15(b)). With around 15% interparticle contacts are parallel to x-direction (see TS in Fig. 13), the isothermal surfaces are still almost perpendicular to x-axis when heat transfers in x-direction (Fig. 15(d)). However, no interparticle contacts are parallel to z-direction, resulting in the isothermal surfaces in the middle of TS are not perpendicular to the z-direction, shown in Fig. 15(e). Therefore, the angle θ' indicates the inclination of an edge along direction B away from the real temperature gradient direction in contrast with angle θ which present the inclination of the edge away from the vertical direction. As shown in Fig. 15(e), θ' is larger than θ and it might be better to be used to penalise the resistance at local contacts, resulting in in smaller local resistances and a smaller sample-scale R. Then the penalised R using θ' could enable the R-λ_{eff} relationship in TS matches the general inversely proportional trend. However, in a randomly-distributed sphere sample used in our previous paper [26], as shown in Fig. 16, the simulated isothermal surfaces are still perpendicular to the main heat transfer direction in general. Hence, θ will still be used to compute the local thermal resistance at each network edge and to investigate the relationship of R and λ_{eff} in randomly distributed sphere packings.

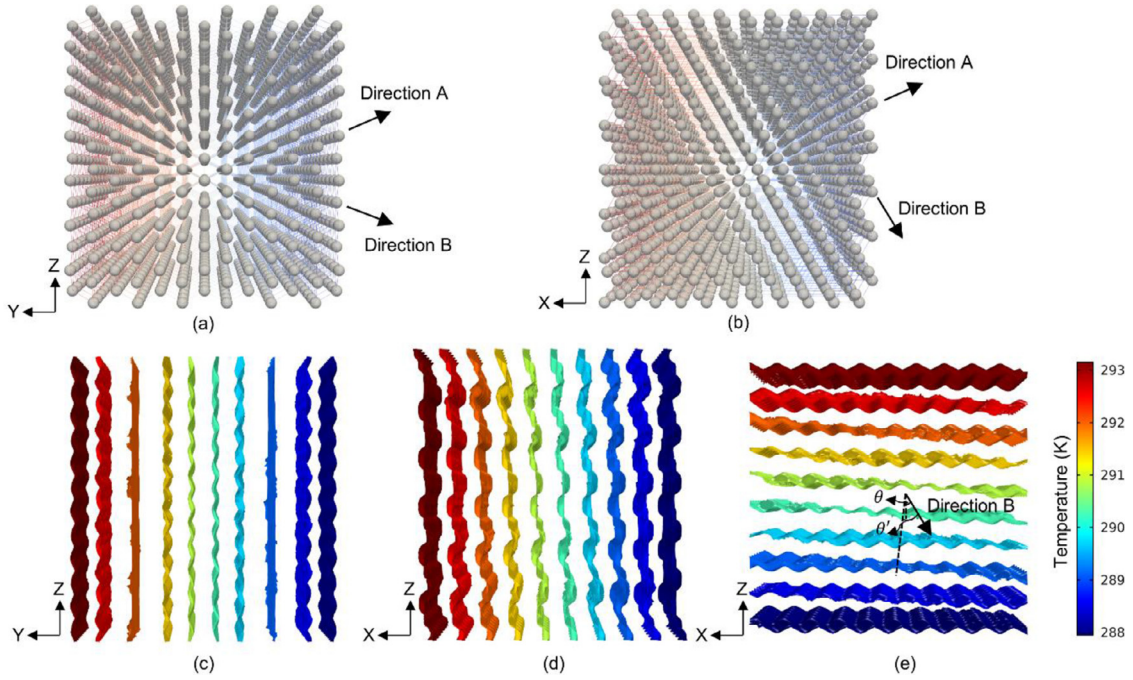

Fig. 15. Illustration of the structure of TS shown in (a) yz and (b) xz view. Note that the particle size is not in scale and the colours of lines in (a) and (b) indicate y and *x* values, respectively. Isothermal surface in TS when heat transfers in (c) y, (d) x and (e) z directions.

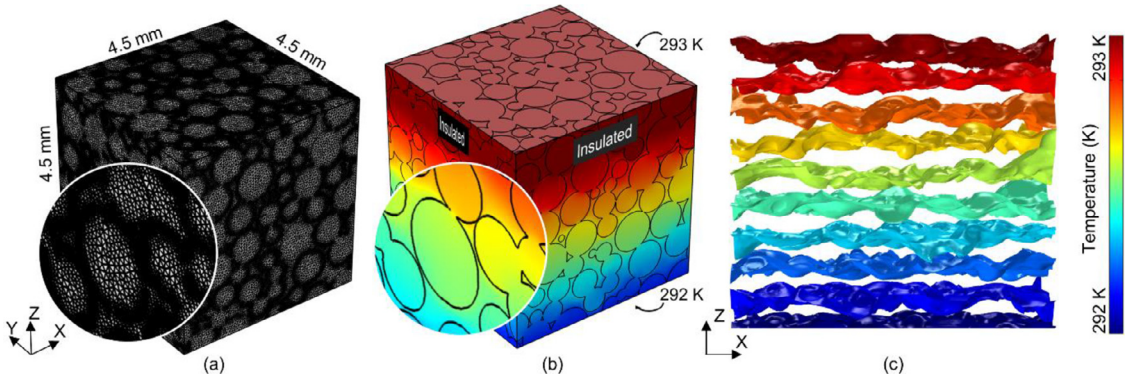

Fig. 16. Randomly-distributed sphere packing: Finite element meshes (a), computed temperature distribution (b) and isothermal surface (c) [26].

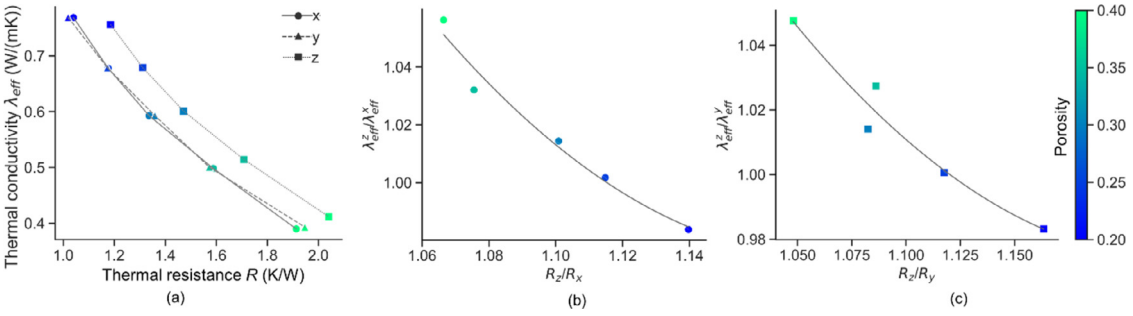

Fig. 17. Thermal anisotropy: Directed network thermal resistance R versus λ_{eff} of randomly distributed sphere packings (a). The ratio of directed network thermal resistance versus thermal anisotropy in x and z directions (b), and in y and z directions (c).

5.4. Directed network thermal resistance and thermal anisotropy in randomly distributed sphere packings

Five randomly distributed sphere packings with porosity of 0.2, 0.25, 0.3, 035 and 0.4 were prepared by compressing a large enough loose cubic sample with a z-directional velocity that is 1.5 times of x and y directional velocity to induce topological anisotropy. The five samples were used to further investigate the feasibility of applying new thermal directional network thermal resistance R to predict λ_{eff} in different directions (i.e, its potential to predict the extent of thermal anisotropy).

In all x, y and z directions, results in Fig. 17(a) still show that λ_{eff} has an inversely proportional correlation with R. The data points are coloured by the porosity of each sample, indicating

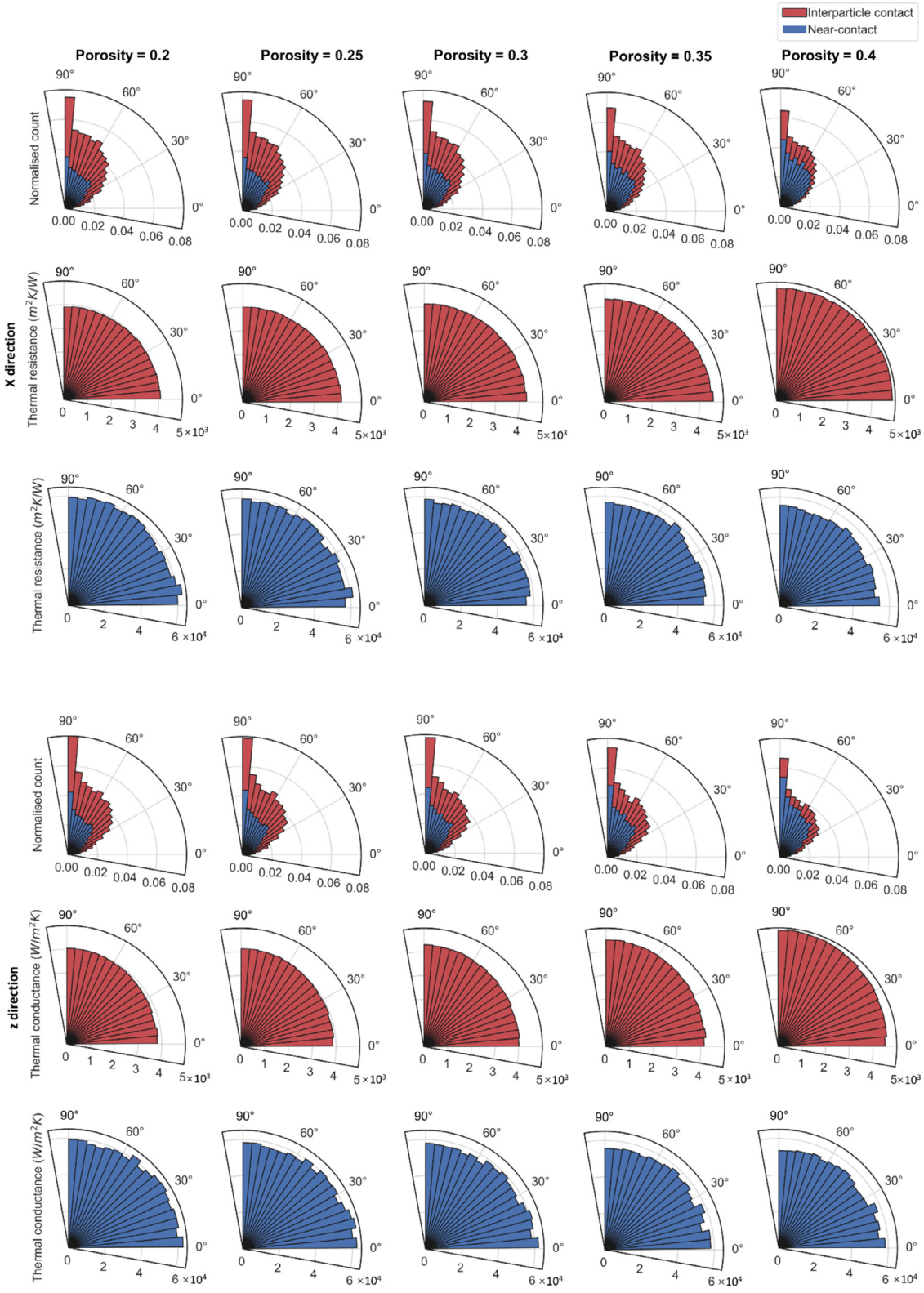

Fig. 18. Contact direction and thermal resistance distribution in randomly distributed sphere pakcings when heat transfers in x and z directions.

that R decrease with the increase of porosity. Compared with that porosity cannot distinguish the difference of λ_{eff} in different directions, the proposed new R shows the advantage of redressing this shortcoming. Fig. 18 shows the contact angle and thermal resistance distribution in different directions. In contact angle distribution at either x and y direction, the red area shrinks while the blue area expands with the increase of porosity, indicating the number of interparticle contacts decreases while that of near-contacts increases. In addition, the thermal resistance at interparticle contacts increases while that at near-contacts decreases.

The ratio of z-directional λ_{eff} to x or y directional λ_{eff}, symbolised as $\lambda^z_{eff}/\lambda^x_{eff}$ and $\lambda^z_{eff}/\lambda^x_{eff}$, are used to quantify the thermal anisotropy. Similarly, directional network thermal resistance ratio R_z/R_x and R_z/R_y are created to examine their correlation with thermal anisotropy. Fig. 17(b) and (c) show R_z/R_x and R_z/R_y are well correlated with thermal anisotropy. In other words, the ratio of R in two different directions can indicate the extent of thermal anisotropy.

6. Conclusions

This work constructed new directed weighted thermal networks by considering (1) topological contacts including interparticle contacts and near-contacts, (2) local thermal resistance at each contact, and (3) contact orientation. These three aspects quantify the three attributes of a contact: (1) particle connectivity, (2) contact quality and (3) contact orientation, respectively. The importance of each attribute to heat transfer was analysed theoretically and numerically. Directed weighted thermal networks were constructed for both lattice sphere packings and randomly distributed sphere packings. From each network, a new sample-scale directed thermal resistance R was extracted and it can encapsulate the three attributes of contacts. Notably, the inlet-outlet thermal resistors representing preferential heat transfer paths are used to compute R. Hence, this new thermal resistance computation approach involves multiple-scale microstructural characterization and can benefit material design for superior thermal properties. The λ_{eff} of each sample is computed using TNM that is verified by results from theoretical models and FEM. The R shows a good correlation with λ_{eff} when heat transfers in different directions. The ratio of R in two different directions can also be used to indicate the extent of thermal anisotropy in the related directions. If gas is confined in small gaps, gas thermal conductivity reduces with the decrease of air pressure. This is known as the Smoluchowski effect and it is important in projects such as packed beds.

Declaration of Competing Interest

The authors declared that there is no conflict of interest.

CRediT authorship contribution statement

Wenbin Fei: Conceptualization, Methodology, Investigation, Software, Validation, Formal analysis, Writing – original draft, Visualization. **Qirui Ma:** Resources, Investigation. **Kenichi Soga:** Conceptualization, Writing – review & editing. **Guillermo A. Narsilio:** Conceptualization, Writing – review & editing, Funding acquisition.

Acknowledgments

The authors acknowledge the funding provided by the Australian Research Council project DP210100433. This research was also supported by use of the Nectar Research Cloud for numerical simulations, this is a collaborative Australian research platform supported by the NCRIS-funded Australian Research Data Commons (ARDC).

References

[1] A. Bidarmaghz, N. Makasis, W. Fei, G.A. Narsilio, An efficient and sustainable approach for cooling underground substations, Tunn. Undergr. Space Technol. 113 (2021) 103986.
[2] Q. Li, W. Fei, J. Ma, M. Jing, X. Wei, Coupled CO_2 sequestration simulation using Abaqus and Eclipse, Environ. Geotech. 40 (2019) 1–10.
[3] D. Ye, G. Liu, F. Gao, R. Xu, F. Yue, A multi-field coupling model of gas flow in fractured coal seam, Adv. Geo Energy Res. 5 (1) (2021) 104–118.
[4] A.R. Peeketi, M. Moscardini, S. Pupeschi, Y. Gan, M. Kamlah, R.K. Annabattula, Analytical estimation of the effective thermal conductivity of a granular bed in a stagnant gas including the Smoluchowski effect, Granul. Matter 21 (4) (2019) 1–21.
[5] G. Buntebarth, Bestimmung Thermophysikalischer Eigenschaften an Opalinustonproben, Geophysikalisch-Technisches Büro, Clausthal-Zellerfeld, 2004.
[6] D. Perić, T.V. Tran, M. Miletić, Effects of soil anisotropy on a soil structure interaction in a heat exchanger pile, Comput. Geotech. 86 (2017) 193–202.
[7] W. Ehlers, C. Luo, A phase-field approach embedded in the theory of porous media for the description of dynamic hydraulic fracturing, Comput. Methods Appl. Mech. Eng. 315 (2017) 348–368.
[8] W. Van Antwerpen, C. Du Toit, P. Rousseau, A review of correlations to model the packing structure and effective thermal conductivity in packed beds of mono-sized spherical particles, Nucl. Eng. Des. 240 (7) (2010) 1803–1818.
[9] Z. Abdulagatova, I. Abdulagatov, V. Emirov, Effect of temperature and pressure on the thermal conductivity of sandstone, Int. J. Rock Mech. Min. Sci. 46 (6) (2009) 1055–1071.
[10] A.M. Abyzov, A.V. Goryunov, F.M. Shakhov, Effective thermal conductivity of disperse materials. I. Compliance of common models with experimental data, Int. J. Heat Mass Transf. 67 (2013) 752–767.
[11] H. Wei, S. Zhao, Q. Rong, H. Bao, Predicting the effective thermal conductivities of composite materials and porous media by machine learning methods, Int. J. Heat Mass Transf. 127 (2018) 908–916.
[12] N. Zhang, H. Zou, L. Zhang, A.J. Puppala, S. Liu, G. Cai, A unified soil thermal conductivity model based on artificial neural network, Int. J Therm. Sci. 155 (2020) 106414.
[13] W. Fei, G.A. Narsilio, M.M. Disfani, Predicting effective thermal conductivity in sand using an artificial neural network with multiscale microstructural parameters, Int. J. Heat Mass Transf. 170 (2021) 120997.
[14] G. Kain, B. Lienbacher, M.-C. Barbu, B. Plank, K. Richter, A. Petutschnigg, Evaluation of relationships between particle orientation and thermal conductivity in bark insulation board by means of CT and discrete modeling, Case Stud. Nondestr. Test. Eval. 6 (2016) 21–29.
[15] R. Askari, S.H. Hejazi, M. Sahimi, Thermal conduction in deforming isotropic and anisotropic granular porous media with rough grain surface, TPM 124 (1) (2018) 221–236.
[16] D. Wang, Z. Liu, J. Shen, W. Liu, Lattice Boltzmann simulation of effective thermal conductivity of porous media with multiphase, J. Porous Media 18 (10) (2015).
[17] X.C. Li, X.Y. Huang, Numerical investigation of thermal conductivity of particle dispersive composites based on fractal method, in: Advanced Materials Research, 616-618, Trans Tech Publications, 2013, pp. 1808–1812.
[18] I.L. Ngo, V.A. Truong, An investigation on effective thermal conductivity of hybrid-filler polymer composites under effects of random particle distribution, particle size and thermal contact resistance, Int. J. Heat Mass Transf. 144 (2019) 118605.
[19] A. Mohamad, Thermal contact theory for estimating the thermal conductivity of nanofluids and composite materials, Appl. Therm. Eng. 120 (2017) 179–186.
[20] J. Choo, Y.J. Kim, J.H. Lee, T.S. Yun, J. Lee, Y.S. Kim, Stress-induced evolution of anisotropic thermal conductivity of dry granular materials, Acta Geotech. 8 (1) (2013) 91–106.
[21] L. Papadopoulos, M.A. Porter, K.E. Daniels, D.S. Bassett, Network analysis of particles and grains, J. Complex Netw. 6 (4) (2018) 485–565.
[22] A. Tordesillas, S.T. Tobin, M. Cil, K. Alshibli, R.P. Behringer, Network flow model of force transmission in unbonded and bonded granular media, Phys. Rev. E 91 (6) (2015) 062204.
[23] J.H. van der Linden, G.A. Narsilio, A. Tordesillas, Machine learning framework for analysis of transport through complex networks in porous, granular media: a focus on permeability, Phys. Rev. E 94 (2) (2016) 022904.
[24] A. Tordesillas, D.M. Walker, Q. Lin, Force cycles and force chains, Phys. Rev. E 81 (1) (2010) 011302.
[25] W. Fei, G.A. Narsilio, Network analysis of heat transfer in sands, Comput. Geotech. 127 (2020) 103773.
[26] W. Fei, G.A. Narsilio, J.H. van der Linden, M.M. Disfani, Network analysis of heat transfer in sphere packings, Powder Technol. 362 (2020) 790–804.
[27] Y. Yu, R. Kerry Rowe, Improved solutions for porosity and specific surface of a uniform porous medium with attached film, J. Environ. Eng. 138 (4) (2012) 436–445.
[28] R. Caulk, L. Sholtès, M. Krzaczek, B. Chareyre, A pore-scale thermo–hydro-mechanical model for particulate systems, Comput. Methods Appl. Mech. Eng. 372 (2020) 113292.
[29] C. Kloss, C. Goniva, A. Hager, S. Amberger, S. Pirker, Models, algorithms and validation for opensource DEM and CFD–DEM, Prog. Comput. Fluid Dyn. Int. J. 12 (2-3) (2012) 140–152.
[30] A. Angus, L.A.A. Yahia, R. Maione, M. Khala, C. Hare, A. Ozel, R. Ocone, Calibrating friction coefficients in discrete element method simulations with shear-cell experiments, Powder Technol. 372 (2020) 290–304.
[31] F. Hernández, P. Pereslavtsev, Q. Kang, P. Norajitra, B. Kiss, G. Nádasi, O. Bitz, A new HCPB breeding blanket for the EU DEMO: evolution, rationale and preliminary performances, Fusion Eng. Des. 124 (2017) 882–886.
[32] Y. Asakuma, Y. Kanazawa, T. Yamamoto, Thermal radiation analysis of packed bed by a homogenization method, Int. J. Heat Mass Transf. 73 (2014) 97–102.
[33] T.S. Yun, J.C. Santamarina, Fundamental study of thermal conduction in dry soils, Granul. Matter 10 (3) (2008) 197–207.
[34] G.K. Batchelor, R. O'brien, Thermal or electrical conduction through a granular material, Proc. R. Soc. Lond. A 355 (1682) (1977) 313–333.

[35] Z. Lai, Q. Chen, L. Huang, Fourier series-based discrete element method for computational mechanics of irregular-shaped particles, Comput. Methods Appl. Mech. Eng. 362 (2020) 112873.
[36] Y. Feng, An effective energy-conserving contact modelling strategy for spherical harmonic particles represented by surface triangular meshes with automatic simplification, Comput. Methods Appl. Mech. Eng. 379 (2021) 113750.
[37] T.S. Yun, T.M. Evans, Three-dimensional random network model for thermal conductivity in particulate materials, Comput. Geotech. 37 (7) (2010) 991–998.
[38] J.H. van der Linden, G.A. Narsillio, A. Tordesillas, Thermal conductance network model for computerised tomography images of real dry geomaterials, Comput. Geotech. (2021) Article No. 104093, PII S0266-352X(21)00097-5, doi:10.1016/j.compgeo.2021.104093.
[39] M. Moscardini, Y. Gan, S. Pupeschi, M. Kamlah, Discrete element method for effective thermal conductivity of packed pebbles accounting for the Smoluchowski effect, Fusion Eng. Des. 127 (2018) 192–201.
[40] S. Suo, M. Moscardini, V. Becker, Y. Gan, M. Kamlah, Cyclic thermo-mechanical performance of granular beds: effect of elastoplasticity, Powder Technol. 394 (2021) 705–713.
[41] R. Penide-Fernandez, F. Sansoz, Microscale Knudsen effect over the transverse thermal conductivity of woven ceramic fabrics under compression, Int. J. Heat Mass Transf. 171 (2021) 121085.
[42] T.P. Peixoto, The graph-tool python library, figshare (2014). https://graph-tool.skewed.de/static/doc/faq.html.
[43] W. Fei, G.A. Narsilio, J.H. van der Linden, M.M. Disfani, Quantifying the impact of rigid interparticle structures on heat transfer in granular materials using networks, Int. J. Heat Mass Transf. 143 (2019) 118514.
[44] COMSOL AB, COMSOL Multiphysics v5.0, https://www.comsol.com/support/knowledgebase/1223, (2015).
[45] A.L. DeVera, W. Strieder, Upper and lower bounds on the thermal conductivity of a random, two-phase material, J. Phys. Chem. 81 (18) (1977) 1783–1790.
[46] J. Sass, A.H. Lachenbruch, R.J. Munroe, Thermal conductivity of rocks from measurements on fragments and its application to heat-flow determinations, J. Geophys. Res. 76 (14) (1971) 3391–3401.
[47] Z. Hashin, S. Shtrikman, A variational approach to the theory of the effective magnetic permeability of multiphase materials, J. Appl. Phys. 33 (10) (1962) 3125–3131.
[48] R. Hill, A self-consistent mechanics of composite materials, J. Mech. Phys. Solids 13 (4) (1965) 213–222.
[49] V. Tarnawski, W. Leong, F. Gori, G. Buchan, J. Sundberg, Inter-particle contact heat transfer in soil systems at moderate temperatures, IJER 26 (15) (2002) 1345–1358.
[50] K.I. Horai, G. Simmons, Thermal conductivity of rock-forming minerals, Earth Planet. Sci. Lett. 6 (5) (1969) 359–368.